Journal of Zhejiang University-SCIENCE A 2026 27(6):598-609
www.jzus.zju.edu.cn; www.springer.com/journal/11582
E-mail: jzus_a@zju.edu.cn

Research Article
https://doi.org/10.1631/jzus.A2500531

Check for updates

Load characteristics and dynamic stability of hydrogen aerostatic gas bearings in turbo-expanders

Chenjie GU[1,2], Songqiang ZHU[1], Zhenyu LIU[2], Limin QIU[3]✉, Yutao LIU[1], Kai FANG[1], Jingfeng LI[1]

[1]*Zhejiang Baima Lake Laboratory Co. Ltd., Hangzhou 310051, China*
[2]*School of Mechanical Engineering, Zhejiang University, Hangzhou 310058, China*
[3]*Institute of Refrigeration and Cryogenics, Zhejiang University, Hangzhou 310027, China*

Abstract: Hydrogen-lubricated bearings are critical components of hydrogen turbo-expanders in large-scale hydrogen liquefaction systems. However, the low viscosity of hydrogen presents significant challenges to the bearing's operational stability, and research on this topic remains limited. Therefore, we investigate the static characteristics of a hydrogen aerostatic gas bearing (HAGB) using a 3D computational fluid dynamics (CFD) model, comparing its performance with that of helium and air bearings. Our analysis reveals that the HAGB primarily operates under the influence of the hydrostatic effect, with its hydrodynamic effect being relatively weak due to hydrogen's low viscosity. Moreover, the impact of the HAGB's operational and structural parameters on its dynamic behavior is investigated. The dynamic stability is evaluated using the dissipated energy and the equivalent damping coefficient. The results indicate that the equivalent damping coefficient can be enhanced by increasing the rotational speed and supply pressure, as well as reducing the gas film clearance. Specifically, in the investigated configuration, the HAGB demonstrates optimal vibration damping when the inlet orifice diameter is 0.2 mm.

Key words: Aerostatic bearing; Hydrogen lubrication; High-speed bearing; Dynamic characteristics; Stiffness and damping

1 Introduction

Hydrogen energy is considered a critical clean energy source for sustainable development because of its abundant reserves, environmental friendliness, and wide applicability. Converting renewable energy sources such as photovoltaic, solar, geothermal, and wind power in remote areas into hydrogen for storage and transportation can mitigate intermittency and fluctuation issues associated with renewable energy generation, and make full use of off-peak and surplus electricity (Incer-Valverde et al., 2022; Noh et al., 2023). As an important energy carrier, hydrogen can extend the applicative scope of renewable energy sources.

However, hydrogen has a low volumetric energy density of under 3 kWh/m^3 at atmospheric pressure, which limits its large-scale storage and transportation over long distances. Liquefaction can increase the density of hydrogen by nearly 800 times. Compared with widely used high-pressure gaseous hydrogen storage, liquid hydrogen features higher energy density and lower storage pressure, thus presenting obvious advantages in storage capacity and safety (Barthelemy et al., 2017; Elberry et al., 2021). The Claude cycle based on hydrogen expansion is the main technical approach for large-scale hydrogen liquefaction systems, and in this process, the high-speed hydrogen turbo-expander is of critical importance (Zhou et al., 2024).

Gas bearings boast advantages such as low friction, long service life, and a wide operating temperature range, and are therefore widely applied in high-speed cryogenic turbo-expanders (Li, 2018; Gao et al., 2019; Wu, 2022). However, due to the low viscosity and compressibility of the gas itself, gas bearings have low load capacity, low stiffness, and poor dynamic stability, and are prone to nonlinear dynamic instabilities such as gas film whirling and oscillation (Qiu et al., 2025). Aerostatic gas bearings can carry loads via a stiff pressurized gas film, which is formed by throttling an external gas supply. Moreover, loads can be manually

✉ Limin QIU, limin.qiu@zju.edu.cn
Chenjie GU, https://orcid.org/0009-0003-2691-3035

Received Oct. 19, 2025; Revision accepted Mar. 9, 2026;
Crosschecked Apr. 24, 2026; Online first June 9, 2026

adjusted to meet operational requirements, yielding better reliability (Chen et al., 2021; Qiang et al., 2023). Aerostatic gas bearings can also provide an additional load by virtue of the hydrodynamic effect when the high-speed rotor is eccentric.

At this point, research on aerostatic gas bearings has largely focused on improving load capacity and gas film stiffness through the optimization of structural and operational parameters, such as orifice holes, gas film clearance, and supply pressure. For example, an aerostatic bearing with helium was designed and analyzed using numerical modeling by Lee et al. (2023). The stiffness and gas consumption of the bearing under different gas supply parameters were investigated, and the appropriate orifice diameter for achieving maximum bearing stiffness was determined. Additionally, the performance of tangentially supplied and radially supplied aerostatic bearings was compared by Qiu et al. (2025). It was found that although the tangentially supplied bearing had a slightly lower load capacity, it could effectively suppress nonlinear subsynchronous vibrations. Moreover, an aerostatic thrust bearing with small feedholes was proposed by Nishio et al. (2011). Through computational fluid dynamics (CFD) simulations and experiments, they concluded that this bearing type had a higher stiffness and damping coefficient than a bearing with compound restrictors. Additionally, Gao et al. (2015) investigated the effects of six orifice chamber configurations on the performance of aerostatic thrust bearings under various operating conditions, presenting a comparison of the load capacity, stiffness, and gas flow rate under the different orifice structures.

Hydrogen's small molecular size, low density, and ultralow viscosity yield a gas film with inferior stiffness and damping properties, compromising the support performance and operational stability of hydrogen bearings compared to conventional helium and air bearings (Gobbato et al., 2011; McDonald, 2012). Aerostatic gas bearings are therefore adopted in hydrogen turbo-expanders to mitigate these limitations. However, their low load capacity and stiffness demand high-precision experiments that are further hindered by explosion risks, thus mostly restricting current research to numerical simulations. Notable numerical studies include that by Qiang et al., (2023), who demonstrated that hydrogen aerostatic thrust bearing load capacity can be enhanced by increasing supply pressure, orifice diameter, and orifice number, reducing gas film clearance, or adding circumferential grooves. Additionally, Yan et al. (2021) proposed a load capacity prediction model for radial hydrogen bearings, yielding analytical calculations consistent with finite difference results. Qiang et al. (2022) further investigated herringbone grooved journal bearings, confirming that hydrogen-lubricated bearings exhibit lower load capacity than those using helium, air, or nitrogen, and pointing to the need for targeted structural optimization. In addition, since the speed of sound in hydrogen is much higher than that in helium and air, the rotor of a hydrogen turbo-expander needs to operate at a higher rotational speed to achieve optimal operating efficiency; this places higher demands on the dynamic characteristics and stability of hydrogen gas bearings at high rotational speeds (Staats, 2008; Wu, 2022).

Existing research on hydrogen gas bearings has predominantly focused on static performance (e.g., load capacity and stiffness), with limited attention being paid to the dynamic characteristics of hydrogen gas films. Hydrogen gas bearings exhibit poor dynamic damping, which weakens the vibration suppression of rotor-bearing systems and exacerbates rotor instability at high rotational speeds. The finite element method (FEM) is widely used to study rotor-bearing vibration characteristics, but requires preacquisition of bearing dynamic stiffness and damping coefficients through simulations or experiments. Lai et al. (2018) adopted a finite element beam model to analyze rotor dynamics, investigating the vibration and response characteristics of gas bearings in cryogenic expanders for air separation systems. Alternatively, fluid–solid coupling models that account for gas film force–rotor interactions can be established to derive dynamic parameters. In one such example, Li et al. (2018) coupled the Reynolds equation with rotor motion equations to build a transient nonlinear model, obtaining rotor center orbits, logarithmic spectra, and Poincaré maps. Moreover, Qiang et al. (2023) introduced small harmonic disturbances into dynamic mesh-based CFD simulations to evaluate the damping dissipation energy, equivalent damping coefficient, and dynamic stiffness coefficients of thrust bearings.

Working fluids for cryogenic turbo-expander gas bearings primarily include air (air separation systems) and helium (reverse Brayton cycle) (Zhou et al., 2022; Liu et al., 2025). The ultralow viscosity of hydrogen poses severe challenges to the dynamic stability and

load-bearing performance of hydrogen aerostatic gas bearings (HAGBs) in hydrogen turbo-expanders. While existing studies have explored the structural design and static performance of these bearings, research on their dynamic characteristics remains limited. In this study, we establish a 3D CFD model of an HAGB to analyze its static characteristics, with the results compared to helium and air bearings. Dynamic characteristic simulations are performed using the dynamic mesh method to derive key dynamic parameters. The impacts of various operating parameters (e.g., disturbance frequency, rotational speed, and supply pressure) and structural parameters (e.g., orifice diameter and gas film clearance) on the HAGB's dynamic parameters and stability are then systematically investigated. Practically, enhancing the high-speed stability of HAGBs may help expand their application to harsh scenarios, such as onshore vibration conditions and hydrogen production on offshore platforms.

2 Numerical simulations

2.1 Governing equations

Flow simulations are conducted on the hydrogen gas film in the aerostatic journal bearing, and the performance of the aerostatic gas bearing is analyzed based on the flow and pressure of the gas film. The simulations are performed using the commercial software ANSYS Fluent. The compressible 3D Navier–Stokes equations are used, and the continuity, momentum, and energy equations are as follows:

$$\frac{\partial \rho}{\partial t}+\nabla\cdot(\rho \boldsymbol{u})=0, \tag{1}$$

$$\frac{\partial}{\partial t}(\rho \boldsymbol{u})+\nabla\cdot(\rho \boldsymbol{u}\boldsymbol{u})=-\nabla P+\mu\nabla^2\boldsymbol{u}, \tag{2}$$

$$\frac{\partial}{\partial t}(\rho h)+\rho \boldsymbol{u}\cdot\nabla h=\frac{\partial P}{\partial t}+\nabla\cdot(k\nabla T), \tag{3}$$

where $\boldsymbol{u}$, ρ, P, μ, and t represent the velocity vector, density, pressure, viscosity, and time, respectively. T, h, and k are the temperature, specific enthalpy, and thermal conductivity, respectively.

The working fluid is treated as an ideal gas considering compressibility. The density, thermal conduction, and viscosity are determined through the ideal gas equation, kinetic theory, and Sutherland law, respectively (Gao et al., 2023).

According to the investigation of Qiang et al. (2023), the flow regime of the thin gas film can no longer be regarded as laminar at high rotational speeds; high speed and high pressure cause the gas to exhibit nonhomogeneity and turbulence within the film clearance. The shear stress transport (SST) k-ω model performs excellently under turbulent flow conditions induced by high supply pressure and high rotational speed, and can accurately predict flow separation and secondary flow in orifice throttling structures. The SST k-ω model is therefore employed in this model, as it has been widely used in calculations of flow fields of gas films in aerostatic gas bearings, in particular due to its accuracy in representing complex shear flows (Cui, 2022; Gao et al., 2023).

2.2 Geometric model

The load capacity of the aerostatic gas bearing is jointly determined by the hydrostatic pressure provided by the throttling of the external gas source, and the hydrodynamic pressure generated by the rotation of the rotor. A schematic diagram of the studied aerostatic journal bearing is shown in Fig. 1. The gas is supplied in two rows, with eight radial gas supply orifices uniformly opened along the circumferential direction in each row. The diameter of the gas supply orifice is represented by d. B_1 is the distance from the orifice to the bearing edge, and ω_r is the rotational speed. θ is used to characterize the pressure distribution of the gas film. The bearing length is B, and the axial location of the supply orifice is at 0.25 times the bearing length. The diameter of the rotor inside the bearing is D, and the average gas film clearance is h_m. During actual operation, the bearing center O and the rotor center O' will be offset, and the offset distance between them is the eccentricity distance e. The eccentricity ratio ε of the bearing is calculated through the average gas film clearance h_m (i.e., $\varepsilon=e/h_m$), since the magnitude of e is much smaller than the rotor diameter D. The structural parameters of the aerostatic journal bearing are presented in Table 1.

Based on the structural parameters above, a 3D gas film model was established to investigate the performance of the HAGB, which was extracted between the journal bearing and the rotor. Owing to the symmetry of the two-row orifice structure, the symmetry plane is set at the axial midpoint of the bearing, and only half of the geometry was used to simplify the

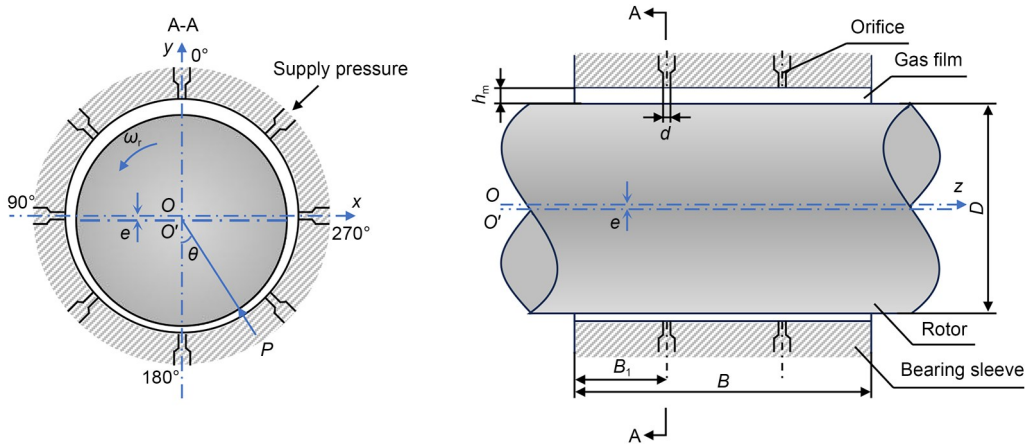

Fig. 1 Schematic diagram of the aerostatic gas bearing

Table 1 Structural parameters of the aerostatic gas bearing

Structural parameter	Value
Bearing width, B (mm)	36
Rotor diameter, D (mm)	25
Orifice position, B_1/B	0.25
Orifice diameter, d (mm)	0.3
Number of orifices per row	8
Number of orifice row	2
Film clearance, h_m (mm)	20

simulation. The depth of the orifice is 1 mm, and an inlet chamber with a radius of 1 mm and a depth of 1 mm is connected to the top of the orifice. Pressurized gas enters the bearing clearance after being throttled through the orifice, and then flows out through the clearance outlet. The 3D flow field in the aerostatic gas bearing with orifice-type restrictors is depicted in Fig. 2.

2.3 Numerical methodology

The boundary conditions are illustrated in Fig. 2. The gas inlet is set with a pressure inlet boundary condition, while the gas outlet is set with a pressure outlet boundary condition. The inner surface of the gas film clearance is the rotor surface, on which a rotating wall boundary condition is applied to simulate the hydrodynamic effect caused by rotor rotation; the shear condition of the rotating wall is assumed to be no-slip. The symmetry plane in the middle of the bearing is configured with a symmetrical boundary condition. The no-slip boundary condition is imposed on the remaining walls.

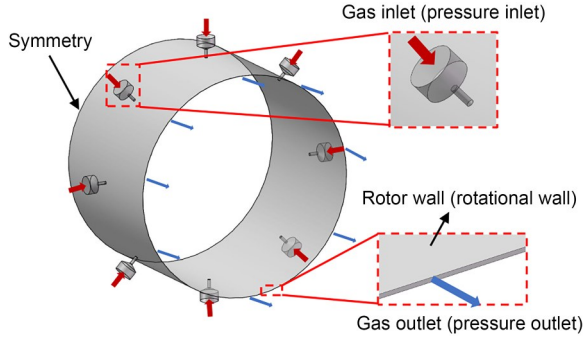

Fig. 2 3D computational domain of the aerostatic gas bearing

Unsteady-state simulations are performed with time steps ranging from 1 to 10 μs to ensure that the Courant–Friedrichs–Lewy condition and convergence are satisfied in each time step. The PRESTO! (pressure staggering option) scheme and the second-order upwind scheme are applied for the spatial discretization of pressure and momentum terms, respectively, to ensure accuracy while reducing computation time. The SIMPLE (semi-implicit method for pressure linked equations) scheme is implemented for pressure–velocity coupling. The calculation is considered to have reached stability when the fluctuation range of the load on the rotor surface is less than 0.1%.

In this study, the eccentricity ratio is adjusted along the y-axis. Thus, the static stiffness coefficient (K_{static}) is characterized by the change in the load capacity along the y-direction, given by Eq. (4). A small eccentricity distance is applied using the dynamic mesh method. The static stiffness coefficient is then calculated based on the change in static load capacity before and after the variation.

$$K_{static} = \frac{\mathrm{d}F_y}{\mathrm{d}e} = \frac{\mathrm{d}F_y}{\mathrm{d}(\varepsilon h_m)}, \tag{4}$$

where F_y represents the gas film load capacities in the y-direction.

Note that dynamic research on HAGBs remains limited. A discussion of the dynamic parameters is included in the electronic supplementary materials (ESM).

The dynamic stability of the bearing–rotor system is the focus of this study. It is assumed that the rotor is only subjected to a small harmonic disturbance in the y-direction, under which only the harmonic vibration of the rotor in the y-direction will appear. The dynamic mesh method is applied to realize the harmonic disturbance of the rotor wall, which in turn characterizes the periodic deformation of the gas film. The harmonic disturbance in the y-direction is expressed as follows:

$$y(t)=Y_1\sin(2\pi nft+\varphi_1), \tag{5}$$

where Y_1 is the amplitude of the disturbance, f is the frequency corresponding to the rotational speed, and φ_1 is the initial phase. n is the dimensionless disturbance frequency, which is the ratio of the disturbance frequency v to the rotational speed frequency f, i.e., $n=v/f$.

The ability of the bearing gas film to dissipate vibrational energy can reflect the stability of the rotor during rotation. Harmonic disturbance, as given in Eq. (6), is applied to the rotor, and the dissipated energy of the gas bearing can be obtained by tracking the load–displacement curve during one cycle of the rotor's displacement. The equivalent damping coefficient is introduced to evaluate the dynamic stability of the rotor, and is calculated from the dissipated energy as follows (Qiang et al., 2023):

$$D_{eq}=\frac{2\Delta E_{dis}}{2\pi nfl^2}, \tag{6}$$

where ΔE_{dis} is the dissipated energy, which is calculated from the enclosed area of the load–displacement curve, and l is the maximum deformation of the gas film.

Also note that more details on the mesh scheme and mesh independence are provided in the ESM.

2.4 Validation of the hydrodynamic model

There are few published experimental data on HAGBs. Here, the static load capacity of an HAGB obtained from measurements by Wu (2022) is used to verify the accuracy of the model. In the experiments, the rotor diameter is 36 mm, and the bearing length is 30 mm. The gas is also supplied in two rows, with 12 orifices in each row and an orifice diameter of 0.3 mm. The supply pressure of hydrogen gas is 0.6 MPa.

A comparison between the simulation results and experimental data is provided in Fig. 3. The simulated results of the load capacity are consistent with the experimental results of Wu (2022). The average deviation between the simulated and experimental results of the load capacity is 2.7%, and the maximum deviation is 7.4%. Therefore, the established flow model can effectively predict the load capacity of the HAGB. The calculation of the dynamic parameters of gas bearings is based on the pressure data at each time step. Consequently, the accuracy of the load capacity can reflect the accuracy of the dynamic parameter calculation to a certain extent. Existing models of gas bearings have also been verified by static load capacity experiments (Gao et al., 2015; Qiang et al., 2023).

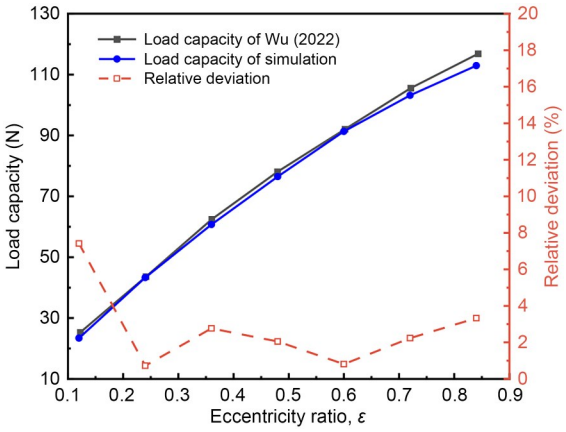

Fig. 3 Load capacity of a hydrogen journal bearing from the simulations and reported experiments

3 Results and discussion

3.1 Static characteristics of the HAGB

The performance of an aerostatic gas bearing is inseparable from the gas lubricant used. The static characteristics of the HAGB were analyzed and compared with those of helium and air applied in cryogenic turbo-expanders. The physical properties of hydrogen, helium, and air at 300 K and 0.6 MPa are listed in Table 2. The typical operational conditions adopted are as follows: an eccentricity ratio of 0.6, a rotational speed of 6×10^4 r/min, and a supply pressure of 0.6 MPa.

Table 2 Physical properties of hydrogen, helium, and air at 300 K and 0.6 MPa

Gas	Density (kg/m^3)	Viscosity (μPa·s)	Compressibility factor
Hydrogen (H_2)	0.48	8.94	1.0006
Helium (He)	0.96	19.95	1.0028
Air	6.98	18.65	0.9982

3.1.1 Effect of eccentricity ratio

The variations in the static characteristics of hydrogen, helium, and air under different eccentricity ratios are summarized in Fig. 4. In Fig. 4a, the static load capacity (F_{static}) at 0 r/min is shown. For all three cases, their static load capacities increase with the rise in eccentricity ratio, although their growth rates gradually decrease. Additionally, the static load capacities of H_2 and air reach their peak when the eccentricity ratio is 0.8, while that of He nearly attain peak at this eccentricity ratio. The static load capacity of hydrogen is lower than that of air but higher than that of helium because of the effect of gas throttling through the orifices and gas compressibility (refer to Table 2). Higher gas compressibility leads to a more pronounced volumetric expansion effect when the gas passes through the orifices into the clearance. The stronger its compressibility is, the more easily it expands, and the more pressure energy will be converted into kinetic energy, thereby reducing the area of the high-pressure region in the gas film. Helium has higher compressibility, so more pressure energy is converted into kinetic energy during throttling, resulting in weaker pressure recovery in the gas film and lower static load capacity.

For a rotor speed of 6×10^4 r/min, the total load capacity (F_{total}), which is obtained by superimposing the dynamic load capacity induced by high-speed rotation onto the static load capacity, is presented in Fig. 4b. It can be observed that under high rotational speeds, the total load capacity of helium exceeds that of hydrogen and is close to that of air; this is attributed to the fact that gas viscosity is a key parameter affecting dynamic load capacity. The pressure gradient within the gas film clearance of helium is larger due to its higher viscosity, leading to a stronger dynamic pressure effect when the rotor rotates at high speeds. The ratio of the static load capacity to the total load capacity (F_{static}/F_{total}) is also illustrated in Fig. 4b. The proportion of the static load capacity of hydrogen is higher than that of helium or

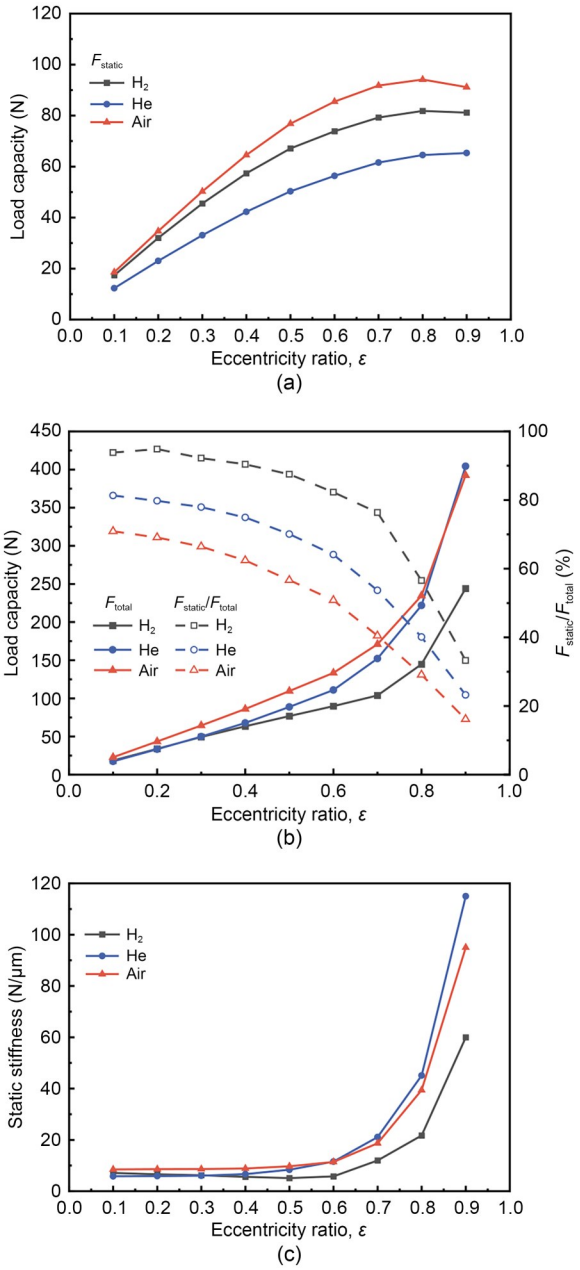

Fig. 4 Static characteristics of gas bearings with different eccentricity ratios: (a) static load capacity; (b) total load capacity; (c) static stiffness

air due to its low viscosity. Specifically, the static load capacity of hydrogen accounts for over 80% when the eccentricity ratio is less than 0.6. Therefore, the operation of hydrogen-lubricated bearings is dominated by the hydrostatic effect. Under low eccentricity ratios, the hydrodynamic effect does not contribute significantly to the improvement of the total load capacity.

The static stiffnesses of gas bearings lubricated with hydrogen, helium, and air are plotted against

eccentricity ratios in Fig. 4c. When the eccentricity ratio is less than 0.5, the gas film stiffness of the three gas bearings is mainly dominated by the hydrostatic effect, and the stiffness varies little with the eccentricity ratio. In these cases, the average static stiffness of hydrogen is lower than that of helium and air by 7.4% and 44.7%, respectively. When the eccentricity ratio exceeds 0.6, the hydrodynamic effect of the gas film becomes significantly enhanced, and the stiffness of the gas bearings increases rapidly with the eccentricity ratio. Owing to the weaker hydrodynamic effect of hydrogen, the increment in stiffness for the hydrogen gas bearing is smaller than that for helium and air bearings. For cases where the eccentricity ratio is above 0.6, the average static stiffness of hydrogen is lower than that of helium and air by 93.7% and 65.3%, respectively.

The circumferential and axial pressure distribution curves of the HAGB were also extracted, which are presented and discussed in the ESM.

3.1.2 Effect of rotational speed

The variation in load capacity and stiffness under varying rotational speeds for aerostatic gas bearings with the three different gases as lubricants is presented in Fig. 5. When the rotational speed of the HAGB increases from 0 to 1×10^5 r/min, its total load capacity rises by 31.7%, which is far lower than the corresponding increases for helium (127.1%) and air (86.5%). Even when the rotational speed reaches 1×10^5 r/min, the proportion of static load capacity in the HAGB only amounts to 66.9%. Therefore, it is difficult to significantly improve the load capacity of the HAGB by increasing the rotational speed to enhance the hydrodynamic effect.

The static stiffness of the HAGB at 1×10^5 r/min increases by 345.1% compared to the case at 0 r/min. The static stiffness of the HAGB at high rotational speeds is much lower than that of helium and air bearings because of its weak hydrodynamic effect. For helium, its static stiffness exhibits the most significant increase with greater rotational speed, with the increase ratio reaching 590.4%—this is due to its high viscosity. It can be concluded that the hydrodynamic effect, as affected by gas viscosity, exerts a significant influence on the improvement of static stiffness. Meanwhile, due to its inherently low viscosity, hydrogen is more prone to operational instability under high-speed operating conditions.

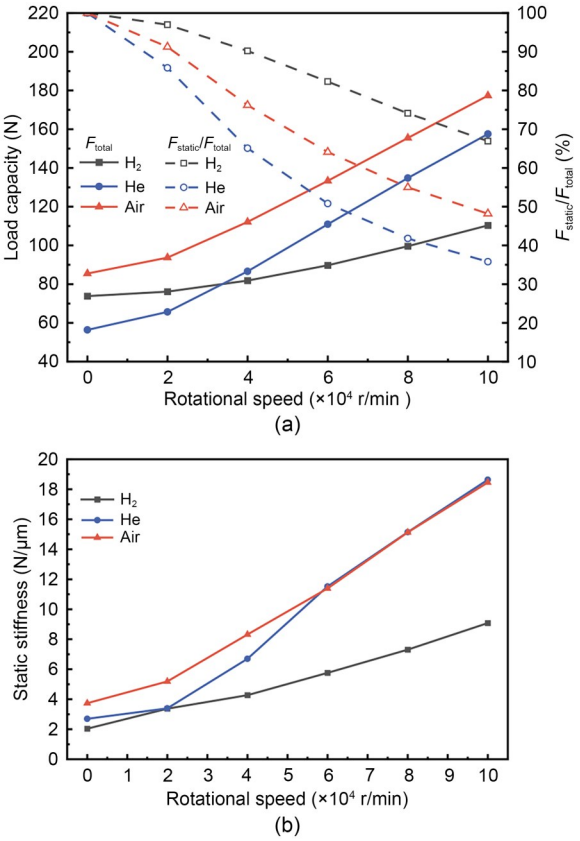

Fig. 5 Static characteristics of gas bearings with different rotational speeds: (a) total load capacity; (b) static stiffness

3.1.3 Effect of supply pressure

The load capacity and static stiffness of the gas bearings are plotted against the supply pressure (P_0) in Fig. 6. When the supply pressure is 1.0 MPa, the increase in the total load capacity of the HAGB compared to the case at 0.2 MPa reaches 342.4%, which is far higher than the increases of 154.8% for helium and 150.0% for air.

The gas supply from orifice restrictors is the main source of the hydrostatic effect. Thus, increasing the supply pressure has a strong improvement effect on the load capacity of the HAGB. Even when the rotational speed reaches 6×10^4 r/min, the proportion of static load capacity in the HAGB at 1.0 MPa is as high as 93.2%, indicating that the hydrostatic effect is dominant. Moreover, the static stiffness of the HAGB grows by 86.3%, which is higher than the increases of 24.9% for helium and 55.8% for air within the calculation range. Therefore, the static stiffness of the HAGB can be improved by increasing the supply pressure. Notably, the gain in the static stiffness of the HAGB from

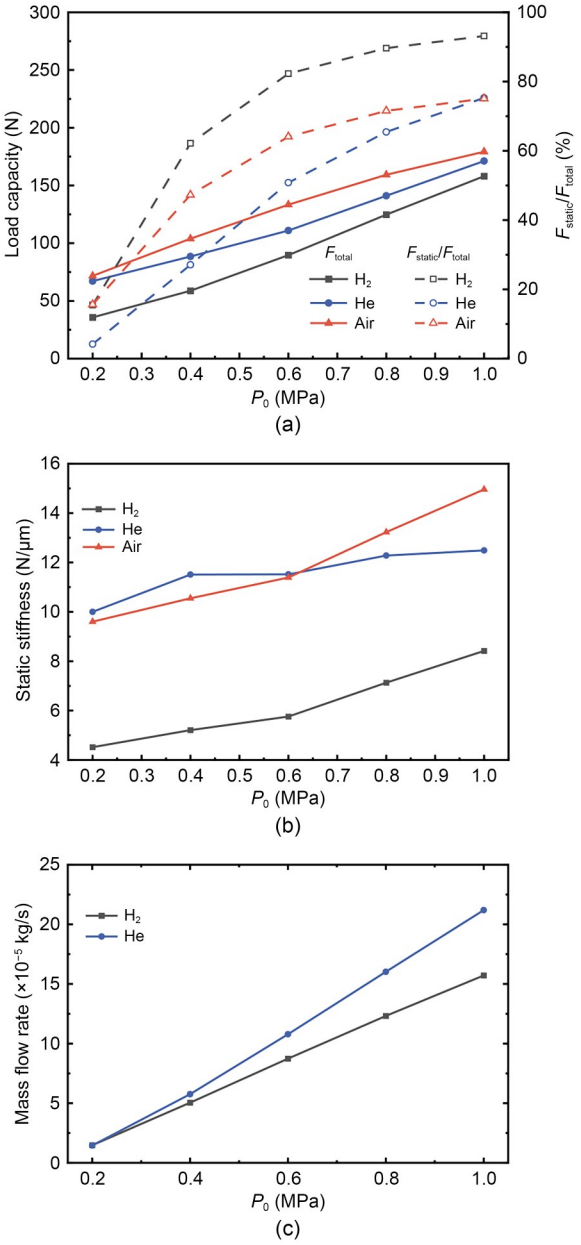

Fig. 6 Static characteristics of gas bearings with different supplied pressures: (a) total load capacity; (b) static stiffness; (c) mass flow rate

increasing the rotational speed is low. Even though the supply pressure causes a large increase ratio for static stiffness, its value is still much lower than that of helium and air bearings when the rotational speed is 6×10^4 r/min, as illustrated in Fig. 6b.

Admittedly, increasing the supply pressure will raise both the gas consumption and the power requirement of the external gas supply equipment. Therefore, a suitable supply pressure should be determined in accordance with the actual operating conditions. Fig. 6c presents the variation in the mass flow rates of the HAGB and the helium gas bearing with the supply pressure. At 0.2 MPa, the gas consumption of the HAGB and the helium gas bearing are almost the same. As the supply pressure increases, the mass flow rates of both the HAGB and the helium gas bearing increase linearly, but the growth rate of the mass flow rate for the HAGB is lower than that for the helium gas bearing. Accordingly, the supply pressure of gas bearings in hydrogen turbo-expanders can be slightly higher than that for helium turbo-expanders, a fact that is widely leveraged in small- and medium-sized hydrogen liquefaction systems.

3.2 Effects of operational parameters on stability

From the above analysis, we can conclude that the load capacity of the HAGB is dominated by the hydrostatic effect. Its hydrodynamic effect is relatively weak under high rotational speeds, which may reduce stability under high-speed operation. Next, the dynamic stability of the HAGB is analyzed. The operational conditions that we adopt remain as follows: an eccentricity ratio of 0.6, a rotational speed of 6×10^4 r/min, and a supply pressure of 0.6 MPa.

Fig. 7 presents the variation curves of the gas film load during one cycle of rotor vibration as a function of the dimensionless disturbance frequency n, rotational speed, and supply pressure. As n increases, the maximum gas film load capacity gradually increases, while the minimum gas film load capacity gradually decreases, leading to an expansion of the load fluctuation range. Fig. 7b shows that increasing the rotational speed enhances the hydrodynamic effect of the HAGB, thus improving the overall load capacity of the HAGB. The maximum and minimum load capacities at 1×10^5 r/min increase by 37.0% and 21.6%, respectively, compared to those at 2×10^4 r/min. The increase in the maximum load capacity is higher than that of the minimum load capacity. Fig. 7c shows that as the supply pressure increases, the load–displacement curve shifts upward as a whole, and the range of the load capacity significantly expands. Within the calculated range, the maximum and minimum load capacities increase by 510.4% and 724.2%, respectively.

The dissipated energy and equivalent damping coefficient can more intuitively reflect the dynamic stability of gas bearings. The dissipated energy is calculated from the area under the load–displacement curve.

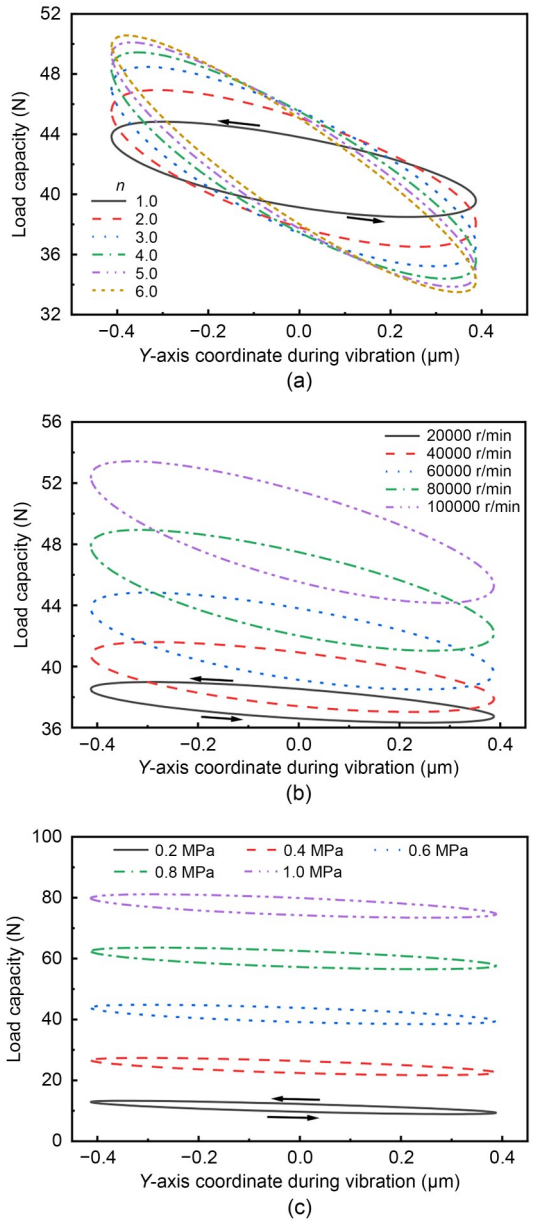

Fig. 7 Variations in dynamic load for varying (a) disturbance frequency, (b) rotational speed, and (c) supply pressure

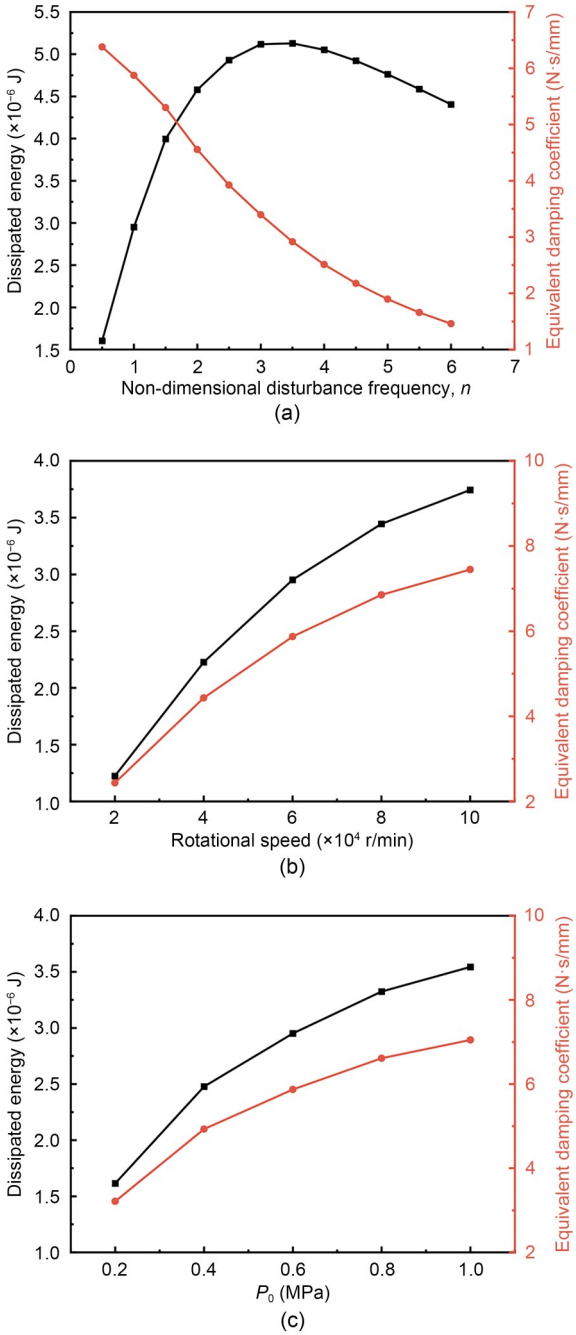

Fig. 8 Variation in dissipated energy and equivalent damping coefficient with (a) disturbance frequency, (b) rotational speed, and (c) supply pressure

The results are presented in Fig. 8, showing the variation in the dissipated energy and equivalent damping coefficient with dimensionless disturbance frequency n, rotational speed, and supply pressure. In Fig. 8a, the dissipated energy first increases and then decreases with n, reaching a peak value at n=3; the equivalent damping coefficient decreases gradually with n. Therefore, the dynamic stability of the HAGB is weakened as the disturbance frequency increases. Increasing the rotational speed and supply pressure of the HAGB can enhance the hydrodynamic effect and hydrostatic effect, respectively, thereby improving the fluid shear dissipation capability. Therefore, in Figs. 8b and 8c, both the dissipated energy and equivalent damping coefficient increase as the rotational speed and supply pressure increase. The increases in these operational parameters enhance the ability to dissipate vibrational energy and improve dynamic stability.

3.3 Effects of structural parameters on stability

Next, we investigated the effects of the structural parameters of the orifice diameter and gas film clearance on the dynamic characteristics. The impact of structural parameter adjustments on the dynamic characteristics of the HAGB was analyzed, which clarified directions for the optimization of these parameters. The operational conditions for the simulations are consistent with those in earlier sections.

The load–displacement curves of HAGBs with different orifice diameters and gas film clearances are presented in Fig. 9. Looking at Fig. 9a, as the orifice diameter increases, the overall load capacity range of the HAGB gradually decreases. The maximum and minimum load capacities decrease by 22.0% and 24.0% as the orifice diameter increases from 0.15 to 0.35 mm, respectively. In Fig. 9b, the enclosed area of the curves decreases with the increase in the gas film clearance within the calculation range. As the gas film clearance increases from 15 to 25 μm, both the maximum and minimum load capacities grow, increasing by 6.0% and 37.4%, respectively. Although the load ranges of the curves at 25 and 30 μm are comparable, the maximum and minimum values of these two curves decrease and increase by 1.6% and 0.9%, respectively. It is worth noting that the hydrodynamic effect is significantly enhanced when the gas film clearance is 10 μm, resulting in the load–displacement curve having the largest load capacity range and the largest enclosed area; this is consistent with the earlier analysis on gas film clearance.

The variational trends of the dissipated energy and equivalent damping coefficient with the orifice diameter and gas film clearance are shown in Fig. 10. Fig. 10a shows that the dissipated energy and equivalent damping coefficient first increase and then decrease with the orifice diameter, reaching a peak when the orifice diameter is 0.2 mm. Thus, the HAGB can best dissipate vibrational energy when the inlet orifice diameter is 0.2 mm. Additionally, the dissipated energy and equivalent damping coefficient trend downward as the gas film clearance increases. Because of the low viscosity of hydrogen, the inherent hydrodynamic effect of the

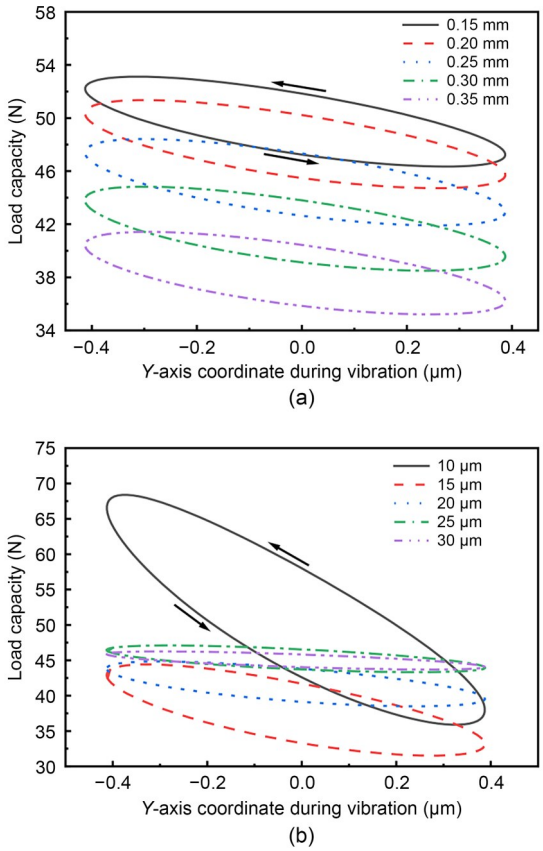

Fig. 9 Variation in dynamic load for different (a) orifice diameters and (b) gas film clearances

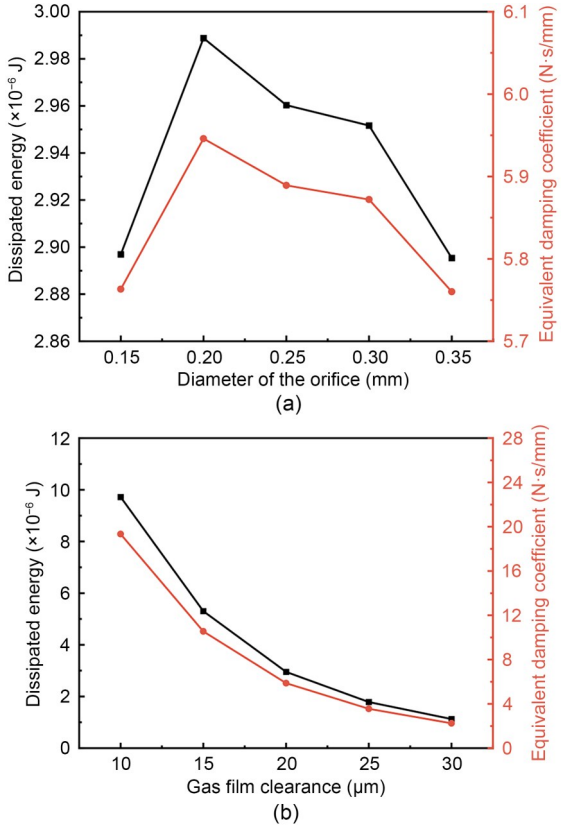

Fig. 10 Variation in dissipated energy and equivalent damping coefficient with (a) orifice diameter and (b) gas film clearance

HAGB is weak, but it can be enhanced by reducing the gas film clearance. Moreover, reducing the gas film clearance will not weaken the hydrostatic effect, thereby improving the dynamic stability of the HAGB.

4 Conclusions

In this study, 3D CFD simulations were performed to study the flow and static characteristics of HAGBs. Using a dynamic mesh method, the dynamic characteristics under harmonic disturbances were investigated, and the influence of operational and structural parameters on the dynamic stability was analyzed.

We found that compared with helium and air bearings, the HAGB shows unique static performance due to hydrogen's low viscosity. The HAGB's load capacity was higher under the same working conditions, indicating dominance of the hydrostatic effect. Although increasing the eccentricity ratio and rotational speed enhances the hydrodynamic effect in gas bearings, this effect remains weak in an HAGB, making the improvement in load capacity and stiffness less obvious than in helium and air bearings. Increasing the supply pressure raises the HAGB's load capacity and stiffness, but these quantities are still lower than those of helium and air bearings, mainly due to the weak hydrodynamic effect. Moreover, it was revealed that increased disturbance frequency lowers the equivalent damping and reduces stability. In contrast, higher rotational speeds and supply pressures enhance vibrational energy dissipation and equivalent damping, thus improving dynamic stability. The vibrational energy dissipation and equivalent damping first increase and then decrease with orifice diameter, reaching an optimum at 0.2 mm for the considered bearing configuration. Importantly, reducing the gas film clearance can compensate for the weak hydrodynamic effect of an HAGB, and further enhance its dynamic stability. Therefore, to optimize the dynamic stability of an HAGB, priority should be given to increasing the supply pressure and reducing the gas film clearance within appropriate ranges. Meanwhile, the optimal orifice size and design can be determined through simulations.

Acknowledgments

This work is supported by the Science and Technology Program of Zhejiang Province (No. 2024SSYS0065), China.

Author contributions

Chenjie GU: methodology, software, formal analysis, and writing–original draft. Yutao LIU: project administration. Jingfeng LI: software and validation. Songqiang ZHU: supervision and writing–review & editing. Zhenyu LIU: writing–review & editing. Limin QIU: supervision and conceptualization. Kai FANG: funding acquisition.

Conflict of interest

Chenjie GU, Songqiang ZHU, Zhenyu LIU, Limin QIU, Yutao LIU, Kai FANG, and Jingfeng LI declare that they have no conflict of interest.

Declaration on the use of generative AI tools

During the preparation of this work, the authors used ChatGPT to improve language and readability. After using this tool, the authors reviewed and edited the content as needed and take full responsibility for the content of the publication.

Data availability

The data that support the findings of this study are available from the corresponding author upon reasonable request.

References

Barthelemy H, Weber M, Barbier F, 2017. Hydrogen storage: recent improvements and industrial perspectives. *International Journal of Hydrogen Energy*, 42(11):7254-7262. https://doi.org/10.1016/j.ijhydene.2016.03.178

Chen SX, Zhang QY, Fu B, et al., 2021. Analysis of static and dynamic characteristics of aerostatic bearing with reflux orifices. *Industrial Lubrication and Tribology*, 73(6):961-970. https://doi.org/10.1108/ILT-05-2021-0166

Cui W, 2022. Research on Static and Dynamic Characteristics and Flow Field Supersonic Characteristic of Micro-Groove-Orifice Aerostatic Journal Bearing Under High Gas Supply Pressure. PhD Thesis, Northeast Forestry University, Harbin, China (in Chinese).

Elberry AM, Thakur J, Santasalo-Aarnio A, et al., 2021. Large-scale compressed hydrogen storage as part of renewable electricity storage systems. *International Journal of Hydrogen Energy*, 46(29):15671-15690. https://doi.org/10.1016/j.ijhydene.2021.02.080

Gao Q, Chen WQ, Lu LH, et al., 2019. Aerostatic bearings design and analysis with the application to precision engineering: state-of-the-art and future perspectives. *Tribology International*, 135:1-17. https://doi.org/10.1016/j.triboint.2019.02.020

Gao QH, Sun WJ, Zhang JZ, 2023. Prediction of aerodynamic and thermal performances for gas foil journal bearing with an axial cooling throughflow by machine learning method. *Thermal Science and Engineering Progress*, 44:102044. https://doi.org/10.1016/j.tsep.2023.102044

Gao SY, Cheng K, Chen SJ, et al., 2015. CFD based investigation on influence of orifice chamber shapes for the design

of aerostatic thrust bearings at ultra-high speed spindles. *Tribology International*, 92:211-221. https://doi.org/10.1016/j.triboint.2015.06.020

Gobbato P, Masi M, Toffolo A, et al., 2011. Numerical simulation of a hydrogen fuelled gas turbine combustor. *International Journal of Hydrogen Energy*, 36(13):7993-8002. https://doi.org/10.1016/j.ijhydene.2011.01.045

Incer-Valverde J, Patiño-Arévalo LJ, Tsatsaronis G, et al., 2022. Hydrogen-driven Power-to-X: state of the art and multi-criteria evaluation of a study case. *Energy Conversion and Management*, 266:115814. https://doi.org/10.1016/j.enconman.2022.115814

Lai TW, Guo Y, Zhao Q, et al., 2018. Numerical and experimental studies on stability of cryogenic turbo-expander with protuberant foil gas bearings. *Cryogenics*, 96:62-74. https://doi.org/10.1016/j.cryogenics.2018.10.009

Lee D, Lim H, Kim B, et al., 2023. Rotordynamic analysis and operating test of an externally pressurized gas bearing turbo expander for cryogenic applications. *Lubricants*, 11(6):252. https://doi.org/10.3390/lubricants11060252

Li J, 2018. Research on Static and Dynamic Characteristics of Bearing-Rotor System of Turbo-Expander in Cryogenic System. PhD Thesis, Huazhong University of Science and Technology, Wuhan, China (in Chinese).

Li J, Yang SQ, Li XM, et al., 2018. Effects of surface waviness on the nonlinear vibration of gas lubricated bearing-rotor system. *Shock and Vibration*, 2018(1):8269384. https://doi.org/10.1155/2018/8269384

Liu HM, Zuo JS, Qiu S, et al., 2025. Simulative and experimental analysis of high-speed helium turbo-expanders in a 5t/day hydrogen liquefier. *International Journal of Hydrogen Energy*, 133:152-164. https://doi.org/10.1016/j.ijhydene.2025.04.403

McDonald CF, 2012. Helium turbomachinery operating experience from gas turbine power plants and test facilities. *Applied Thermal Engineering*, 44:108-142. https://doi.org/10.1016/j.applthermaleng.2012.02.041

Nishio U, Somaya K, Yoshimoto S, 2011. Numerical calculation and experimental verification of static and dynamic characteristics of aerostatic thrust bearings with small feed-holes. *Tribology International*, 44(12):1790-1795. https://doi.org/10.1016/j.triboint.2011.07.004

Noh H, Kang K, Seo Y, 2023. Environmental and energy efficiency assessments of offshore hydrogen supply chains utilizing compressed gaseous hydrogen, liquefied hydrogen, liquid organic hydrogen carriers and ammonia. *International Journal of Hydrogen Energy*, 48(20):7515-7532. https://doi.org/10.1016/j.ijhydene.2022.11.085

Qiang MC, Zhao Q, Yan SH, et al., 2022. Performance prediction of high-speed hydrogen gas-lubricated herringbone grooved journal bearing. *Applied Sciences*, 12(13):6432. https://doi.org/10.3390/app12136432

Qiang MC, Liu MZ, Zhao Q, et al., 2023. Feasibility analysis of adopting the hydrogen hydrostatic thrust bearing. *Applied Sciences*, 13(16):9372. https://doi.org/10.3390/app13169372

Qiu S, Ke CL, Li KR, et al., 2025. Nonlinear dynamic analysis of a novel tangentially supplied aerostatic bearing-rotor system: theory and experiment. *Mechanical Systems and Signal Processing*, 224:112221. https://doi.org/10.1016/j.ymssp.2024.112221

Staats WL, 2008. Analysis of a Supercritical Hydrogen Liquefaction Cycle. MS Thesis, Massachusetts Institute of Technology, Cambridge, USA.

Wu JZ, 2022. Research on Dynamics Characteristics of Bearing-Rotor System of Hydrogen Turbo-Expander. MS Thesis, China Academy of Launch Vehicle Technology, Beijing, China (in Chinese).

Yan H, Ke CL, Peng N, et al., 2021. Performance prediction of externally pressurized gas bearings for high-speed turbo-expander involving hydrogen, helium and air working fluids. *International Journal of Hydrogen Energy*, 46(67):33453-33467. https://doi.org/10.1016/j.ijhydene.2021.07.160

Zhou KM, Li SF, Zhao K, et al., 2022. Efficiency control of the cooling-down process of a cryogenic helium turbo-expander for a 2 t/d hydrogen liquefier. *International Journal of Hydrogen Energy*, 47(69):29794-29807. https://doi.org/10.1016/j.ijhydene.2022.06.275

Zhou KM, Zhao K, Chen L, et al., 2024. High-efficiency control strategies of a hydrogen turbo-expander for a 5 t/d hydrogen liquefier. *Energy*, 297:131326. https://doi.org/10.1016/j.energy.2024.131326

Electronic supplementary materials

Sections S1–S3